Characterization of Bimanual Cyclical Tasks From Single-Trial EEG-fNIRS Measurements

Yi-Chuan Jiang, *Graduate Student Member, IEEE*, Rui Ma, Shichen Qi, Sheng Ge, *Member, IEEE*, Ziqi Sun, Yishu Li, Jongbin Song, and Mingming Zhang, *Senior Member, IEEE*

***Abstract*— Robot-assisted bimanual training is promising to improve motor function and cortical reorganization for hemiparetic stroke patients. Closing the rehabilitation training loop with neurofeedback can help refine training protocols in time for better engagements and outcomes. However, due to the low signal-to-noise ratio (SNR) and non-stationary properties of neural signals, reliable characterization of bimanual training-induced neural activities from single-trial measurement is challenging. In this study, ten human participants were recruited conducting robot-assisted bimanual cyclical tasks (in-phase, 90° out-of-phase, and anti-phase) when concurrent electroencephalography (EEG) and functional near-infrared spectroscopy (fNIRS) were recorded. A unified EEG-fNIRS bimodal signal processing framework was proposed to characterize neural activities induced by three types of bimanual cyclical tasks. In this framework, novel artifact removal methods were used to improve the SNR and the task-related component analysis (TRCA) was introduced to increase the reproducibility of EEG-fNIRS bimodal features. The optimized features were transformed into low-dimensional indicators to reliably characterize bimanual training-induced neural activation. The SVM classification results of three bimanual cyclical tasks revealed a good discrimination ability of EEG-fNIRS bimodal indicators (90.1%), which was higher than that using EEG (74.8%) or fNIRS (82.2%) alone, supporting the proposed method as a feasible technique to characterize neural activities during robot-assisted bimanual training.**

Manuscript received August 11, 2021; revised January 8, 2022; accepted January 10, 2022. Date of publication January 18, 2022; date of current version January 28, 2022. This work was supported in part by the Natural Science Foundation of Shenzhen under Grant JCYJ20210324104203010, in part by the Shenzhen Key Laboratory of Smart Healthcare Engineering under Grant ZDSYS20200811144003009, in part by the National Natural Science Foundation of China under Grant 61903181, and in part by the Guangdong Research Program under Grant 2019ZT08Y191. *(Corresponding author: Mingming Zhang.)*

This work involved human subjects or animals in its research. Approval of all ethical and experimental procedures and protocols was granted by the Ethics Committee of Southern University of Science and Technology under Approval No. 20190004, and performed in line with the Declaration of Helsinki.

Yi-Chuan Jiang, Rui Ma, Shichen Qi, Ziqi Sun, Yishu Li, Jongbin Song, and Mingming Zhang are with the Shenzhen Key Laboratory of Smart Healthcare Engineering, Department of Biomedical Engineering, Southern University of Science and Technology, Shenzhen 518055, China (e-mail: zhangmm@sustech.edu.cn).

Sheng Ge is with the Key Laboratory of Child Development and Learning Science, School of Biological Science and Medical Engineering, Ministry of Education, Southeast University, Nanjing 210096, China.

Digital Object Identifier 10.1109/TNSRE.2022.3144216

***Index Terms*— Bimanual cyclical tasks, electroencephalography (EEG), functional near-infrared spectroscopy (fNIRS), task-related component analysis (TRCA), single-trial analysis.**

I. Introduction

BIMANUAL tasks that involve upper limbs working in a highly coordinated way are prevalent in daily activities. However, for hemiparetic stroke patients, the inefficient control of the infacted upper limb may cause difficulty in performing bimanual tasks, leading to loss of life independence [1]. Recent meta-analysis reports proved that robot-assisted bimanual training could improve kinematic and kinetic performance of bilateral upper extremities [2] and facilitate neural reorganization of peri-infarct cortexes [3].

Robot-assisted bimanual therapy enables repetitive and intensive practice at a relatively low cost [4], [5]. By adding sensing units (e.g., force, torque, pulse and respiration sensors, and surface electromyography, etc.) into robotic systems, rehabilitation training outcomes can be quantitatively evaluated. Xu *et al.* [6] incorporated a Leap Motion sensor into robot-assisted bimanual training system and used the measured kinematic behaviors (including movement duration, peak velocity, and mean tangential velocity) to evaluate training performance. In Darzi *et al.*'s study [7], electromyogram (EMG) and respiration rate were monitored and utilized to assess human participants' training status. These behavior and bio-signal indicators have been proved to be strongly correlated with clinical assessment scales (e.g., Fugl-Meyer scales, FMA upper extremity scales), and can be considered as supplements to clinical assessment [8], [9]. Moreover, these sensory data can also be used as feedback to adapt training protocols to users' status, thereby establishing natural human-machine interactions (HMIs) between human users and rehabilitation robots. Such biofeedback rehabilitation could improve patients' engagements, allowing them to exercise intensively without becoming tired, bored or frustrated. The effects have been verified in clinical studies of hemiplegic patients [10]–[12].

Hemiplegic stroke originates from cerebrovascular accident-caused abnormal blood supply and its recovery is related to neural reorganization of motor systems [13], [14]. Therefore, it is potentially more intuitive to evaluate bimanual rehabilitation outcomes in terms of cerebral blood flow

and brain oscillation than the above-mentioned behavior or bio-signal features. With cost and ease of use in mind, electroencephalography (EEG) and functional near-infrared spectroscopy (fNIRS) are the most suitable noninvasive neuroimaging methods to monitor neural activities during robot-assisted bimanual training. EEG reflects neural activation via measuring electrical potentials generated by cortical post-synaptic currents [15], while fNIRS infers brain activities through hemoglobin concentration changes based on the neurovascular coupling theory [16].

Numerous studies have used EEG and fNIRS to characterize robot-assisted bimanual training outcomes. Gandolfi *et al.* [17] used the changes of EEG power to evaluate upper-limb motor recovery during robot-assisted bimanual training. They found that increased desynchronization of upper alpha (10-12 Hz) and beta (13-30 Hz) rhythms on the motor cortex can serve as good biomarkers to characterize bimanual training outcomes. Li *et al.* [18], [19] employed fNIRS to validate the efficacy of robot-assisted bimanual training. Their results proved that bimanual training could evoke high cerebral activation, which may contribute to motor cortex reorganization. Nevertheless, EEG and fNIRS have their own limitations. EEG is typically limited by the high sensitivity to motion and muscle artifacts [20], rendering it less appropriate to investigate neural activity related to upper-limb movements. While fNIRS is more resistant to motion artifacts and electrical noise than EEG [21], the low temporal resolution impedes its application in capturing rapid neural dynamic responses [22].

In the recent decade, EEG-fNIRS bimodal measurement has been increasingly used in cognitive neural mechanism research [23], neurological disease diagnosis [24], and brain-computer interface (BCI) applications [21], [25]. Hybrid EEG and fNIRS can overcome limitations of either modality (e.g., poor artifact resistance for EEG, and low temporal resolution for fNIRS) [26] and improve the precision of neural status evaluation [21], [23]–[25]. To date, and to the best of our knowledge, only two studies [27], [28] have used EEG-fNIRS bimodal system in measuring neural oscillation and hemodynamic activities during robot-assisted bimanual training. Both studies focused on evaluating bimanual training-induced neural activities at just the group level, in which robust neural activation patterns were obtained by averaging all trials. While admitting that the group-level results have potential to evaluate bimanual training outcomes, there is a pressing need to detect neural activities at the single-trial level so that training protocols can be tuned in time for closed-loop engagements.

Single-trial analysis of neural signals is a common challenge due to the low SNR and high trial-to-trial variability [29]. The physiological artifacts (e.g., ocular, muscular, and cardiac artifacts) and ongoing background neural activities are accounted for the low SNR and high variability of single-trial neural signal [30], [31]. Recently, novel denoising methods and feature extraction techniques have been applied to improve the SNR and extract task-related components from single-trial neural signal. In Ge *et al.* 's study [32], a sinusoidal signal-assisted multivariate empirical mode decomposition method was proposed to denoise single-trial motor imagery data. Asgher *et al.* [33] used the fixed-value modified beer-lambert law method to extract mental load-related neural activities from single-trial fNIRS data. Nazeer *et al.* [34] employed a vector-based phase analysis method to extract finger tapping-related components from single-trial fNIRS measurement. However, the effectiveness of these methods has only been validated in simple cognition or motor tasks. For robot-assisted bimanual training tasks, upper-limb movements induced motion and muscle artifacts and human-machine interactions induced background neural activities can seriously contaminate neural signals, making it more challenging to extract task-related components from single-trial measurement. These two challenges have led to a lack of published literature on the characterization of bimanual training-induced neural activation at the single-trial level. Filling this gap can help construct closed-loop robot-assisted bimanual rehabilitation systems with real-time neurofeedback.

This study proposed a unified framework to characterize bimanual training-induced neural activities from single-trail EEG-fNIRS bimodal measurements. In particular, we used novel artifacts removal methods to reduce the interference of motion and muscle artifacts and improve the SNR. Task-related component analysis (TRCA) method [35] was used to enhance reproducibility of within-class EEG-fNIRS bimodal features so that bimanual training-related components can be reliably extracted. The optimized features were finally transformed into low-dimensional indicators to reliably characterize different types of bimanual cyclical tasks. The effectiveness and robustness of our framework were verified by the within-class similarity of optimized features, the discrimination degree of EEG-fNIRS bimodal indicators, and the classification accuracy of bimanual cyclical tasks.

The rest of this paper is organized as follows. The methods, including experimental procedures, data acquisition and EEG-fNIRS signal processing framework, are presented in Section II. Then, the experimental results are reported in Section III in terms of EEG-fNIRS response evaluation and single-trial analysis. Finally, discussion and conclusions are presented in Sections IV and V, respectively.

II. Materials and Methods

A. Participants

Ten healthy adults (seven males and three females, mean age $= 20.6 \pm 0.8$ years, range 20 – 22 years) participated in this study. None of the recruited participants reported neurological or psychiatric disorders. All of them were confirmed to be right-handed by the Edinburgh Handedness Inventory. Before the experiment, all participants provided written informed consent. This study was approved by the Ethics Committee of Southern University of Science and Technology (20190004).

B. Experimental Prototype

This experiment was carried out in a non-shielded environment. As illustrated in Fig. 1.a, the experimental setup consisted of a custom-made bimanual rehabilitation robot, a visual interface, and an EEG-fNIRS bimodal measurement

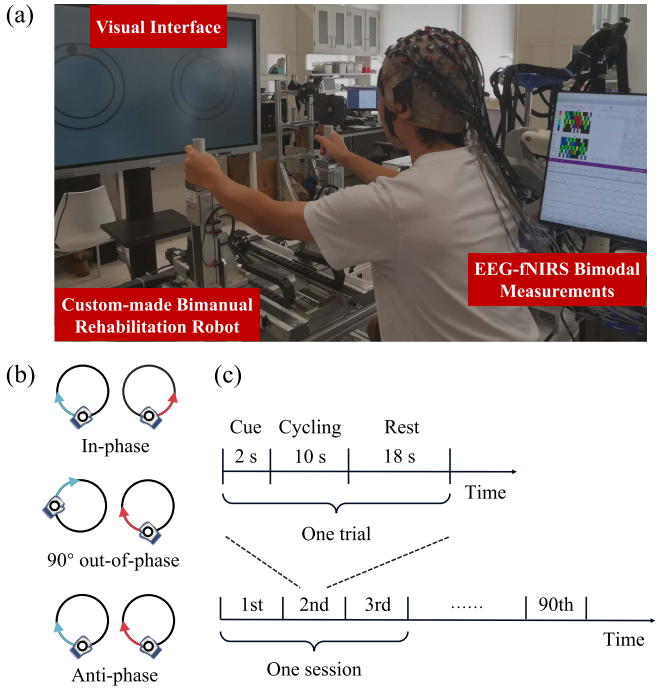

Fig. 1. Experimental setup and procedures. (a) Overall experimental setup, consisted of a visual interface, a custom-made bimanual rehabilitation robot, and an EEG-fNIRS bimodal measurement system. (b) Three kinds of bimanual cyclical tasks: in-phase task, 90° out-of-phase task, and anti-phase task. (c) This experiment included 30 sessions. Each session consisted of 3 trials, during which each kind of bimanual cyclical task was performed once randomly. A single trial had a cue stage for 2 s, a cycling stage for 10 s, and a rest stage for 18 s, respectively.

system. The bimanual rehabilitation robot mainly consisted of two motion modules and a pair of handles. Each motion module was composed of three mutually perpendicular linear actuators. The robotic handle connected to motion module was back-drivable under an admittance control law, allowing three degrees of freedom (DOFs) voluntary movements [36], [37]. Participants were asked to grasp two handles and perform bimanual cyclical tasks (see Section II. C) following visual instruction. We used the Psychophysics Toolbox Version 3 (PTB-3) [38] to control visual cue presentation and synchronize EEG-fNIRS bimodal recording (see Section II. D) via event triggers.

C. Experimental Tasks and Procedures

During the experiment, participants were asked to perform three types of bimanual cyclical tasks (in-phase task, 90° out-of-phase task, and anti-phase task) [39], [40] with the robot in active-resisted mode. (1) In the in-phase task, participants performed outward rotation with the direction symmetrical to the midline of the body (the left hand rotated the handle in a clockwise direction whereas the right hand rotated the handle in a counterclockwise direction); (2) In the 90° out-of-phase task, the initial point of the left hand was 90° ahead of the in-phase mode, and both hands rotated in a clockwise direction; (3) In the anti-phase task, both hands rotated in a clockwise direction. The rotation frequency was set to 0.2 Hz.

As shown in Fig. 1.c, the experiment included 30 sessions. Each session consisted of 3 trials, during which each kind of bimanual task was performed once randomly, resulting in 30 repetitions for each bimanual cyclical task. A single trial included a cue stage for 2 s, a cycling stage for 10 s, and a rest stage for 18 s (see Fig. 1.c).

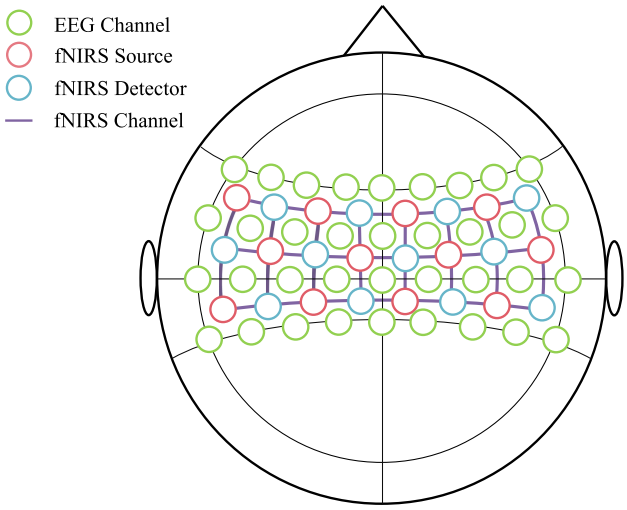

Fig. 2. Arrangement of EEG and fNIRS channels. The EEG electrodes and fNIRS optodes were arranged above the PMC, M1 and S1. Thirty-six EEG electrodes were placed according to the international 10–10 system. A pair of source and detector optodes formed one fNIRS channel. Twelve sources and 12 detectors in the arrangement resulted in a total of 37 channels.

D. Multimodal Data Acquisition

1) EEG: EEG signals were acquired at 1200 Hz using g.Hlamp amplifier (g.tec, Medical Engineering GmbH, Austria). Thirty-six selected EEG electrodes (F7, F5, F3, F1, Fz, F2, F4, F6, F8, FT7, FC5, FC3, FC1, FCz, FC2, FC4, FC6, FT8, T7, C5, C3, C1, Cz, C2, C4, C6, T8, TP7, CP5, CP3, CP1, CPz, CP2, CP4, CP6, TP8) were placed over brain areas associated with bimanual movements, such as premotor cortex (PMC), primary motor cortex (M1) and primary somatosensory cortex (S1), according to the international 10-10 system (see Fig. 2) [41] EEG signals were referenced at the FCz electrode.

2) EOG & EMG: EOG and EMG signals were recorded with the same g.Hlamp amplifier. Two pairs of electrodes were used to record bipolar horizontal and vertical EOG (one pair attached to the external canthi and the other to the infraorbital and supraorbital regions of the right eye), and 4 neck sEMG electrodes (attached to the left and right trapezius and sternocleidomastoid muscles, respectively) were used to monitor electrical muscle activities [42]. EOG and EEG signals were referenced at the FCz electrode and sampled at 1200 Hz.

3) fNIRS: fNIRS signals were recorded simultaneously at 5.21 Hz using a continuous-wave fNIRS neuroimaging system (NIRScout, NIRx Medizintechnik GmbH, Germany). The wavelengths of near-infrared light were 785 nm and 830 nm. fNIRS optodes were covered the participants' PMC, M1 and S1 (see Fig. 2) [43]. The distance between a pair of source and detector was about 3 cm, and each pair formed a fNIRS

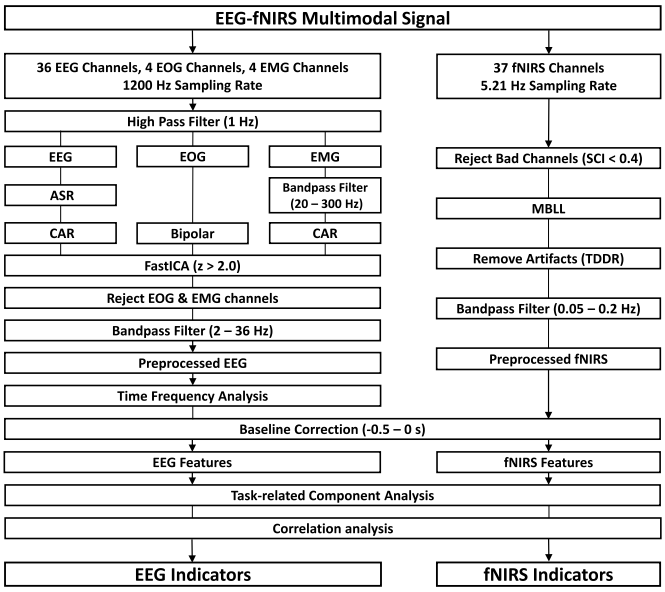

Fig. 3. EEG-fNIRS multimodal signal processing pipeline. It consists of signal preprocessing, feature extraction and optimization, and indicator calculation.

channel. There were 12 sources and 12 detectors in this arrangement, resulting in 37 fNIRS channels.

E. Multimodal Data Processing Pipeline

As shown in Fig. 3, the unified EEG-fNIRS bimodal signal processing framework contains the following three parts: signal preprocessing, feature extraction and optimization, and indicator calculation. The processing of EEG-fNIRS bimodal data was carried out using MNE functions [44] and custom Python scripts.

1) Data Preprocessing:

a) EEG: Thirty-six channel EEG signals, 4 channel EOG signals, and 4 channel EMG signals were first high-passed at 1 Hz to remove low-frequency noise and then separated from each other. For EEG signals, the artifact subspace reconstruction (ASR) algorithm [45] was applied to remove occasional large amplitude artifacts based on statistical criteria from clean EEG. Then, EEG signals were re-referenced using the common averaged reference (CAR) method. For EOG signals, bipolar reference was applied to each electrode pair to extract the vertical and horizontal EOG, respectively. EMG signals were band-pass filtered between 20 and 300 Hz and re-referenced to their common average.

Next, we utilized the fast independent component analysis (FastICA) [46] method to decompose multi-channel EEG signals into several independent components (ICs). ICs with strong correlation (after adaptive z-scoring and thresholding at $Z > 2.0$) with EOG and neck EMG signals were considered responsible for ocular and muscle artifacts and then set to zero before reconstruction. The reconstructed EEG was band-pass filtered between 2 and 36 Hz for further analysis.

b) fNIRS: Raw fNIRS intensity values were first converted into optical density data, and bad channels were rejected based on the scalp coupling index ($SCI < 0.4$) [47]. Next, optical density signals were transformed into the concentration changes of oxyhemoglobin (ΔHbO) and deoxyhemoglobin (ΔHbR) with the modified Beer-Lambert law [48]. We utilized the temporal derivative distribution repair (TDDR) method [49] to correct the baseline shift and spike artifacts caused by head movements. A band-pass filter between 0.05 and 0.2 Hz was applied to obtain preprocessed fNIRS signals.

2) Feature Extraction:

a) EEG: The event-related (de-) synchronization (ERDS) of μ rhythm (8 – 13 Hz), indicating a band power decrease during bimanual movements and an increase during resting period, was used to characterize neuroelectric activities of bimanual cyclical tasks from single-trial EEG recording [50]. Firstly, a 16-second (−2 to 14 s) epoch was extracted from preprocessed single-trial EEG data. The time-frequency representation (TFR) of this epoch was calculated with the *tfr_multitaper* function of MNE-python. Next, we employed the baseline-normalized event-related spectrum perturbation (ERSP) [51] to represent the differences of frequency band power as a function of time, which can be calculated by the following formula:

$$ERSP\,(k,\,f,\,t) = 10\log\frac{|TFR\,(k,\,f,\,t)|^2}{\frac{1}{M}\sum_{m=1}^{M}|TFR\,(k,\,f,\,m)|^2} \tag{1}$$

where $TFR\,(k,\,f,\,t)$ denotes the spectral estimation of channel k at frequency f and time t. M and m indicate the number of discrete-time points and the time point index of baseline period (−0.5 to 0 s). Finally, the task-related variations of μ activities can be calculated by averaging $ERSP$ values of all frequencies in this band, resulting in spectral features ($x_{EEG} \in \mathbb{R}^{K' \times T'}$) of the corresponding single-trial EEG data, where K' and T' denote the number of EEG channels and time points, respectively.

b) fNIRS: The task-related variations of oxygen consumption were employed to characterize neural responses induced by bimanual cyclical task from single-trial fNIRS measurement. Similarly, a 16-second (−2 to 14 s) epoch was extracted from preprocessed single-trial fNIRS data, and the mean value of baseline period (−0.5 to 0 s) was subtracted from this epoch for baseline alignment. fNIRS temporal features ($x_{fNIRS} \in \mathbb{R}^{K'' \times T''}$) can be directly represented as ΔHbO of this epoch, where K'' and T'' indicate the number of fNIRS channels and time points, respectively.

3) Feature Optimization With Task-Related Component Analysis:

The particular problem of single-trial analysis is that the SNR of single-trial data is too weak to extract reliable task-related components for robust analysis. Thus, spatial filtering approaches, such as beamformer, canonical correlation analysis (CCA), and common spatial pattern (CSP), have been used to calculate subject-specific spatial filters for data enhancement [52].

Recently, TRCA [35] was introduced as a novel spatial filtering approach for fNIRS [53] and EEG [54] data analysis. The goal of TRCA is to optimize the coefficients by maximizing the covariance between each pair of within-class training

trials to obtain the task-specific spatial filter. By applying the trained TRCA filter, we can extract a temporal profile of the task-related component that exhibits maximal temporal similarity among within-class training trials. Unlike beamformer and CCA, which assume that templates averaged from training data as source signals, TRCA is entirely data-driven and has no prior assumptions. The optimization process of TRCA is also more interpretative and less aggressive than CSP. In Duan *et al.*'s study [55], TRCA has been demonstrated to be more effective than CCA and CSP in extracting premovement components from EEG data.

In the current study, we introduced TRCA to increase the reproducibility of within-class EEG-fNIRS features and extract bimanual cyclical task-related components for reliable characterization of neural activation during task period. As for each bimanual cyclical task and measurement mode, the corresponding spatial filter $\omega \in \mathbb{R}^{1\times K}$ was constructed by maximizing the inter-trial covariance of task-related components $\omega \in \mathbb{R}^{N\times T}$, where K is the number of channels, N is the number of training trials, and T is the number of time points.

The inter-trial covariance of the n_1-th and n_2-th trial's estimated task-related components can be calculated as follows:

$$\begin{aligned} C_{n_1,n_2} &= Cov\left(Y^{(n_1)}, Y^{(n_2)}\right) \\ &= Cov\left(wX^{(n_1)}, wX^{(n_2)}\right) \\ &= \sum_{k_1,k_2=1}^{K} w_{k_1} w_{k_2} Cov\left(X_{k_1}^{(n_1)}, X_{k_2}^{(n_2)}\right) \end{aligned} \tag{2}$$

where $X \in \mathbb{R}^{K\times N\times T}$ is calculated features of training trials, and $X_k^{(n)}$ denotes features of n-th trial and k-th channel.

All possible combinations from all the training trials are summed as:

$$\begin{aligned} \sum_{\substack{n_1,n_2=1 \\ n_1\neq n_2}}^{N} C_{n_1,n_2} &= \sum_{\substack{n_1,n_2=1 \\ n_1\neq n_2}}^{N} \sum_{k_1,k_2=1}^{K} w_{k_1} w_{k_2} Cov\left(X_{k_1}^{(n_1)}, X_{k_2}^{(n_2)}\right) \\ &= \boldsymbol{w^T S w} \end{aligned} \tag{3}$$

Here, the symmetric matrix $\boldsymbol{S}$ is defined by:

$$S_{k_1,k_2} = \sum_{\substack{n_1,n_2=1 \\ n_1\neq n_2}}^{N} Cov\left(X_{k_1}^{(n_1)}, X_{k_2}^{(n_2)}\right) \tag{4}$$

To obtain a finite solution, the covariance of Y is constrained as:

$$\begin{aligned} Var\,(Y) &= Cov\,(Y, Y) \\ &= \sum_{k_1,k_2=1}^{K} w_{k_1} w_{k_2} Cov\left(X_{k_1}, X_{k_2}\right) \\ &= \boldsymbol{w^T Q w} \\ &= 1 \end{aligned} \tag{5}$$

The constrained optimization problem becomes a Rayleigh-Ritz eigenvalue problem:

$$\widehat{\boldsymbol{w}} = arg\max_{\boldsymbol{w}} \frac{\boldsymbol{w^T S w}}{\boldsymbol{w^T Q w}} \tag{6}$$

The optimal coefficient vector is obtained as an eigenvector of the matrix $\boldsymbol{Q^{-1}S} \in \mathbb{R}^{K\times K}$. K eigenvalues and eigenvectors can be obtained by solving the eigenvalue problem. The task-related components are arranged in a descending order of eigenvalues, and the eigenvector $\omega_{max} \in \mathbb{R}^{1\times K}$ corresponding to the maximum eigenvalue λ_{max} was chosen to be the optimal spatial filter. By repeating this process, the optimal TRCA filter ω_j^i can be calculated for each bimanual cyclical task $i \in$ {in-phase, 90° out-of-phase, anti-phase} and measurement mode $j \in$ {EEG, fNIRS}.

Therefore, the optimized feature of the n-th training trial can be calculated by multiplying training features $X_j^{i(n)}$ with corresponding TRCA filter ω_j^i, and the robust feature template $P_j^i \in \mathbb{R}^{1\times T}$ can be obtained by averaging all combinations of within-class optimized training features, as follows:

$$P_j^i = \frac{1}{N}\sum_{n=1}^{N} \omega_j^i X_j^{i(n)} \tag{7}$$

where N and n denote the number of training trials and the training trial index.

4) Indicator Calculation With Correlation Analysis: We further utilized the correlation coefficient value ρ_j^i between optimized features of test trial T and trained feature template P_j^i as indicators to characterize bimanual training-induced neural activity in low dimensional space, which can be calculated as follows:

$$\rho_j^i = corr\left(\omega_j^i T_j, P_j^i\right) \tag{8}$$

Thereby, the neural activities of each test trial can be represented by only six correlation coefficient indicators (three for EEG, and three for fNIRS).

F. Performance Evaluation

We first evaluated the EEG and fNIRS responses during the task period and compared the differences of bimodal features for three types of bimanual cyclical task. The average method (unweighted average features across channels) was chosen as a comparison to verify the effectiveness of TRCA (weighted average features across channels) in spatial filtering and task-related component extraction. Because the optimization goal of TRCA is extracting reproducible components from training features, we used the within-class similarity S_j^i to measure the reliability of optimized training features, which is defined by averaging correlation coefficients between optimized training features and corresponding feature template:

$$S_j^i = \frac{1}{N}\sum_{n=1}^{N} corr\left(\omega_i^j X_i^{j(n)}, P_j^i\right) \tag{9}$$

We also used the differentiation degree D_j^i to measure the discrimination ability of test indicators, which obtained by summing the inter-cluster distances, as follows:

$$D_j^i = \sum_{l=1,l\neq i}^{I} dist\left(C_j^l, C_j^i\right) \tag{10}$$

where $dist$ is the mean Euclidean distance between all pairs of indicators in the target indicator cluster C_j^i and non-target indicator cluster C_j^l.

Moreover, three kinds of widely-used classification method including linear discriminant analysis (LDA), support vector machine (SVM), and random forest (RF) were employed to evaluate the robustness and stability of calculated indicators. The dataset was divided into a training set and a test set. EEG-fNIRS bimodal trials in the training set were used to obtain TRCA filters and feature templates. Reference indicators calculated by optimized training features and feature templates were used as input for classifier training. This study compared the classification accuracy of EEG, fNIRS, and EEG-fNIRS bimodal indicators with different number of training sizes (from 5 to 15 with a step of one). For each size of the training set, fifty times cross-validation was adopted to obtain a sensible estimate of the classification accuracy.

Statistical analyses were conducted with the one-way analysis of variance (ANOVA) using SPSS software (IBM SPSS Statistics 26.0, IBM Corporation, USA). All post-hoc pairwise comparisons were Bonferroni corrected.

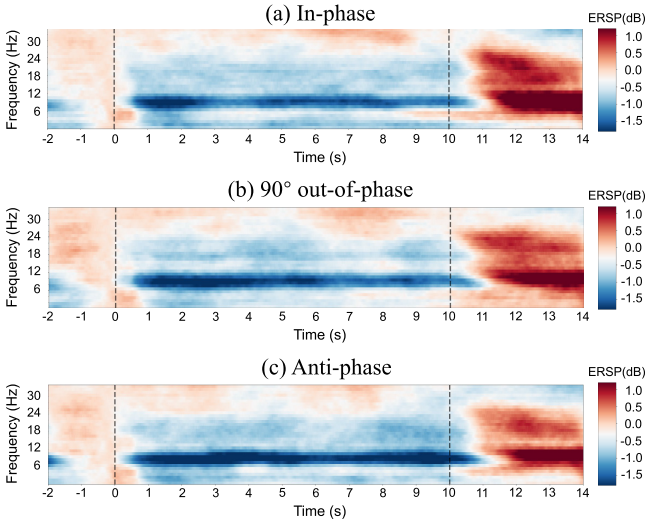

Fig. 4. Grand average of ERSP spectrograms across all channels and all participants for (a) in-phase, (b) 90° out-of-phase, and (c) anti-phase bimanual cyclical tasks. Two vertical dashed lines represent the onset and offset of the tasks, respectively. Apparent ERD phenomenon of μ rhythm (8–13 Hz) can be observed during the task period.

III. Results

A. EEG Response Evaluation

Fig. 4 shows the grand-averaged ERSP spectrograms of in-phase, 90° out-of-phase, and anti-phase bimanual cyclical tasks. The time-frequency maps present an apparent decrease of μ rhythm (8 – 13 Hz) power during task period (0 to 10 s), as well as an increase during rest stage. This ERDS phenomenon can be observed in all three bimanual tasks, especially clear for the anti-phase task.

The ERDS pattern for different types of bimanual cyclical task can be obtained by averaging ERSP values across all frequencies in μ band (see Fig. 6. a). We used the ANOVA to measure the differences of ERDS value across three bimanual tasks, which showed statistically significant differences around 3 s ($F_{(2,897)} = 3.055$, $p = 0.048$) and 9 s ($F_{(2,897)} = 5.545$, $p = 0.004$). The ERDS intensity of anti-phase task was lower than that of in-phase task and 90° out-of-phase task during the task period, while the difference between in-phase task and 90° out-of-phase task can hardly be distinguished.

B. fNIRS Response Evaluation

Fig. 5 shows the group-level topographical distributions of HbO responses for in-phase, 90° out-of-phase, and anti-phase bimanual cyclical tasks. We can observe a typical increase of HbO during bimanual cyclical tasks. The activation at the M1 was more prominent than at other areas.

Fig. 6. b is the grand-averaged HbO responses across all trials. The ANOVA results showed a significant difference in HbO amplitude across three bimanual cyclical tasks from 4 s to 10 s (the lowest $F_{(2,897)} = 12.790$, $p < 0.001$). The averaged peak amplitude of in-phase, 90° out-of-phase, and anti-phase task was 6.2 $\mu mol/L$ at 5.3 s, 6.3 $\mu mol/L$ at 6.1 s, and 14.8 $\mu mol/L$ at 5.5 s, respectively. They peaked around 5.5 s, and the peak amplitude of anti-phase task was significantly higher than that of in-phase task ($p < 0.001$) and 90° out-of-phase task ($p < 0.003$). However, the post-hoc t-tests indicated no significant difference between anti-phase and 90° out-of-phase task ($p = 0.075$), and between in-phase mode and 90° out-of-phase task ($p = 1.000$).

C. Correlation Analysis of Optimized Training Features

Fig. 7 shows the calculated EEG-fNIRS bimodal features and their correlation coefficient values of the first 10 training trials from Subject 2 using the average method and TRCA, respectively. The left column of each subgraph shows the optimized features for three types of bimanual cyclical tasks, and the bold black line is the corresponding training template. The right column shows the cross-correlation coefficients of all training features. Compared with the average method (see Fig. 7. a & c), EEG and fNIRS optimized features calculated by TRCA (see Fig. 7. b & d) were more consistent and the within-class correlation coefficient (within the black box) were larger, which demonstrated that TRCA could extract reproducible task-related components from EEG-fNIRS bimodal features. Moreover, the correlation coefficient values between different bimanual cyclical tasks calculated by TRCA were smaller than that of the average method, which proved that these extracted components were not only reproducible but also task-dependent.

Table I lists the averaged within-class similarity of optimized training features for each bimanual cyclical task and measurement mode. For the average method, the averaged within-class similarity of EEG and fNIRS optimized features were 0.507 and 0.386, respectively. For TRCA method, the averaged within-class similarity of EEG and fNIRS optimized features were 0.660 and 0.676, respectively. The increase of within-class similarity demonstrated the efficacy of the TRCA method in EEG-fNIRS bimodal feature optimized.

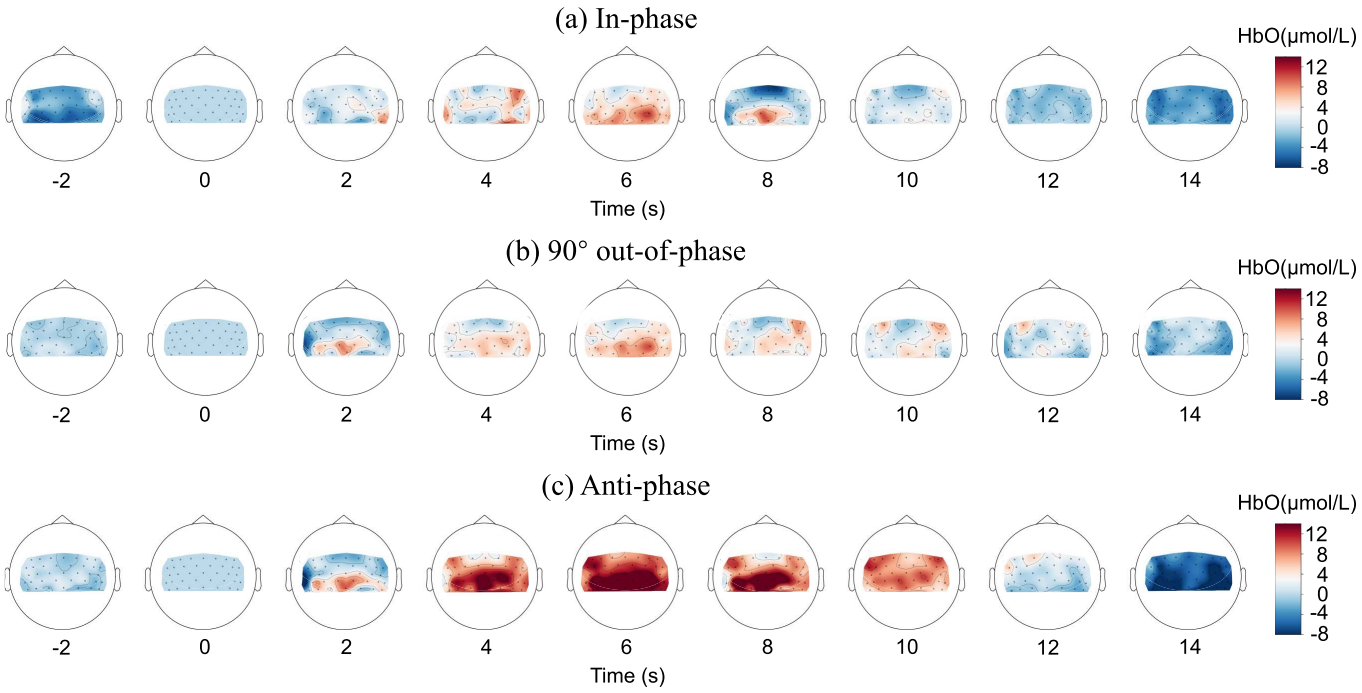

Fig. 5. Grand-averaged topographical distributions of hemodynamic responses across all participants for (a) in-phase, (b) 90° out-of-phase, and (c) anti-phase bimanual cyclical tasks. The red and blue colors indicate high and low hemodynamic activations, respectively. Significant increase of HbO concentration can be observed during the task period (0–10 s).

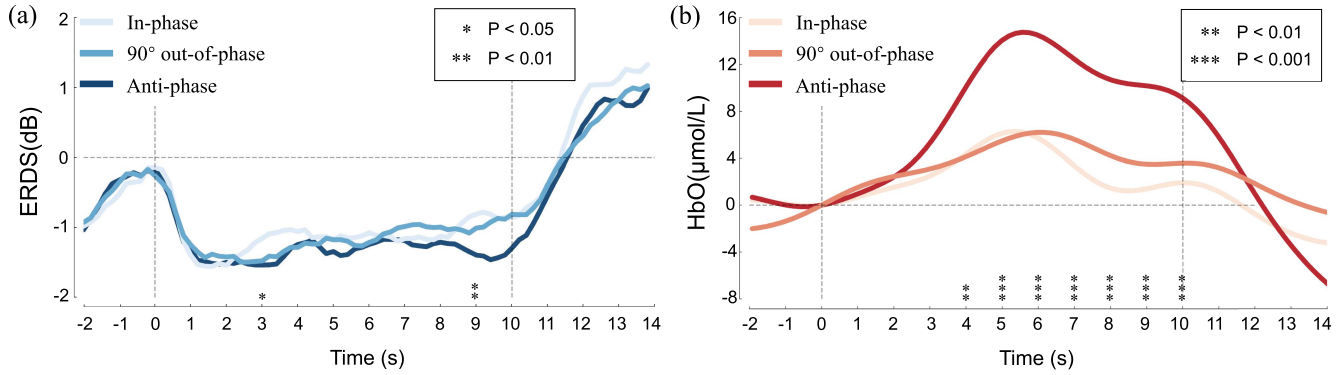

Fig. 6. Group-level time-course of (a) ERDS and (b) HbO responses for three different bimanual cyclical tasks. Two vertical dashed lines indicate the onset (t = 0 s) and offset (t = 10 s) of bimanual tasks. Asterisks denote statistically significant differences in the response amplitude of the bimanual cyclical tasks ($* p < 0.05$, $** p < 0.01$, and $*** p < 0.001$).

D. Discriminative Analysis of Indicators

Fig. 8 shows the indicator distribution of the last 20 test trials from Subject 2 using the average method and TRCA, respectively. The coordinate values of each dot are the correlation coefficient between optimized test trial features and template features (see Eq. 8). As shown in Fig. 8, indicators of different bimanual cyclical tasks calculated by the average method were confusing. While the distribution of within-class indicators calculated by TRCA was more concentrated.

Table II lists the averaged discrimination degree of test indicators for each bimanual cyclical task and measurement mode. For the average method, the averaged discrimination degree of EEG and fNIRS indicators were 1.017 and 1.921, respectively. For TRCA method, the averaged within-class similarity of EEG and fNIRS optimized features were 1.673 and 2.338, respectively. The high discrimination degree proved that the calculated indicators have good characterization ability.

E. Classification Accuracy

Fig. 9 illustrates the averaged classification accuracy across all subjects with different number of training trials. In general, the classification accuracy increased with the number of training trials, and the highest accuracy was obtained when the number of training trials was 15. For EEG indicators, the highest accuracy of RF, LDA, and SVM were 72.1%, 74.1%, and 74.8%, respectively. For fNIRS indicators, the highest accuracy of RF, LDA, and SVM were 77.7%, 81.8%, and 82.2%, respectively. For EEG-fNIRS bimodal indicators, the highest accuracy of RF, LDA, and SVM were 88.3%, 88.2%, and 90.1%, respectively. One-way repeated ANOVA showed

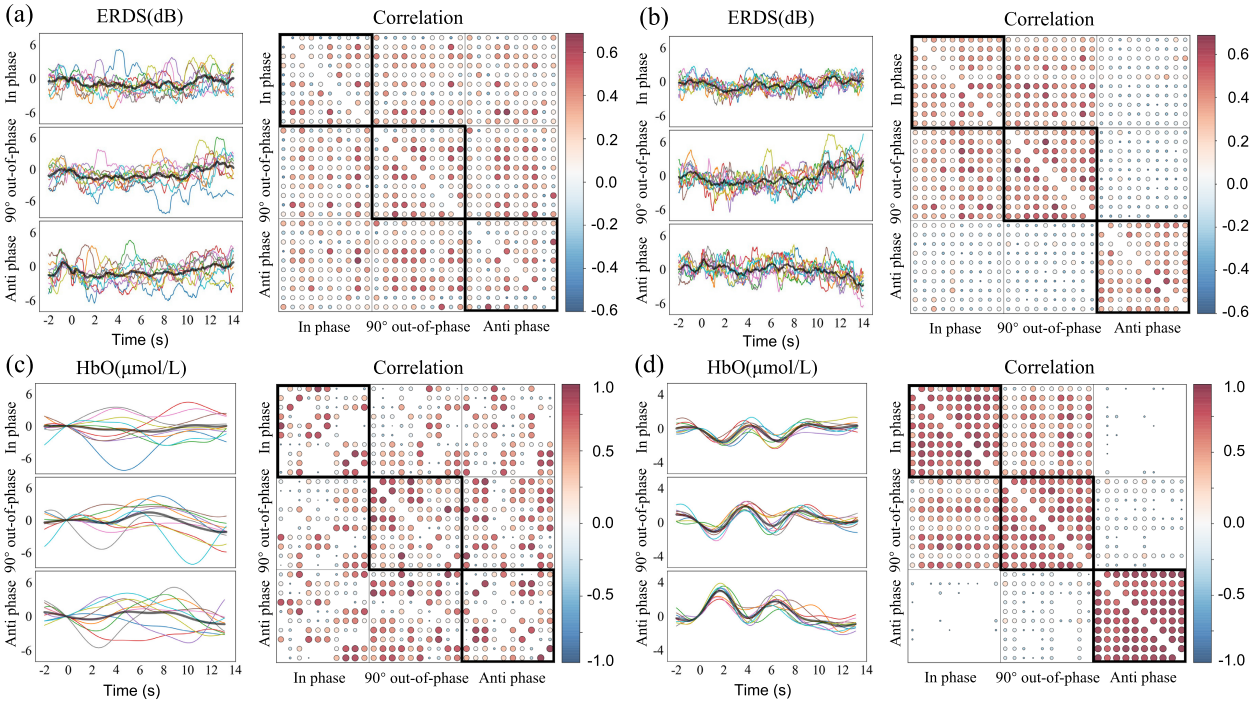

Fig. 7. Comparison of optimized training features and feature templates from Subject 2. (a) EEG features calculated by the average method. (b) EEG features calculated by TRCA. (c) fNIRS features calculated by the average method. (d) fNIRS features calculated by TRCA. The left column of each subgraph illustrates the features of first 10 training trials for three different bimanual cyclical tasks, and the black bold line is the training template calculated using the averaging method or TRCA. The right column shows the cross-correlation coefficients of all training features in the left column, and the correlation coefficients in the black box are the cross-correlation coefficients of single-class training features. The size and color depth of each dot represent the magnitude of coefficient value. The autocorrelation coefficients on the main diagonal and the correlation coefficients less than -0.6 were zeroed out for clear display.

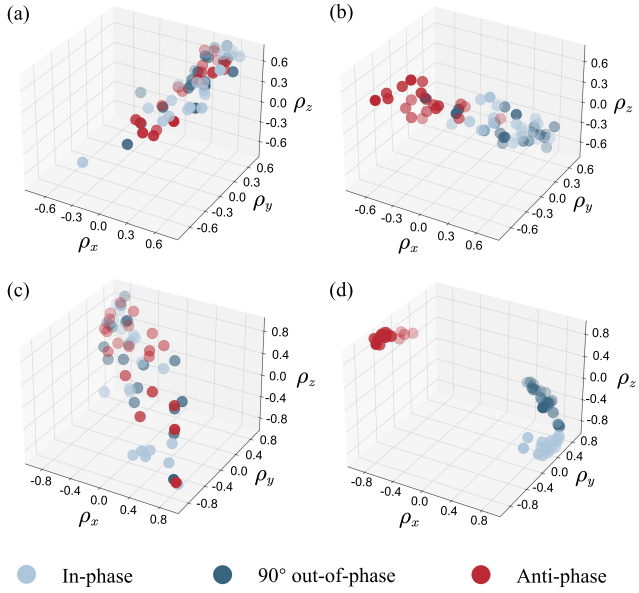

Fig. 8. Indicator distribution of the last 20 test trials from Subject 2. (a) EEG indicators calculated with the average method. (b) EEG indicators calculated with TRCA. (c) fNIRS indicators calculated with the average method. (d) fNIRS indicators calculated with TRCA. The coordinate value of each dot is the correlation coefficient between the test trial feature with the template feature of in-phase (ρ_X), 90° out-of-phase (ρ_Y) and anti-phase (ρ_Z).

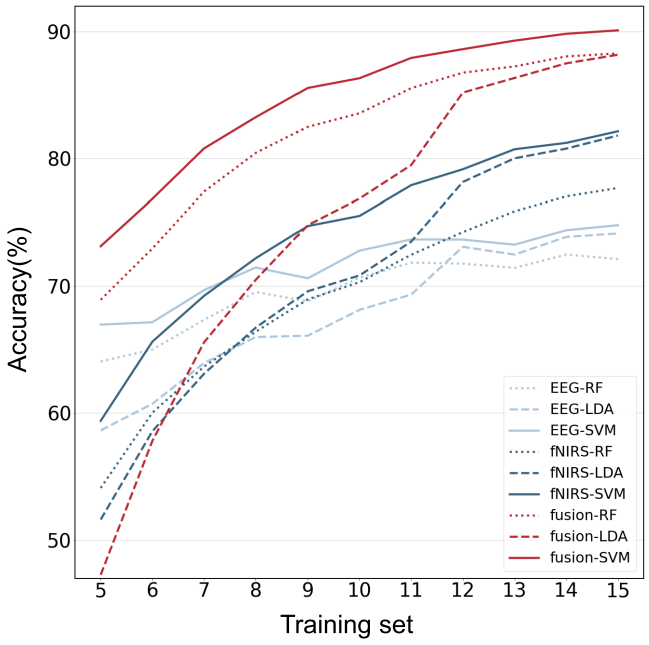

Fig. 9. Averaged across subjects with different numbers of training trials for EEG, fNIRS, and EEG-fNIRS bimodal indicators.

there was a significant difference of the highest accuracy between different types of indicators (RF: $F_{(2,29)} = 8.366$, $p = 0.001$; LDA: $F_{(2,29)} = 6.534$, $p = 0.005$; SVM: $F_{(2,29)} = 8.265$, $p = 0.002$). There was no significant difference of the highest accuracy between different classifiers (EEG indicators: $F_{(2,29)} = 0.364$, $p = 0.698$; fNIRS indicators: $F_{(2,29)} = 0.585$, $p = 0.564$; EEG-fNIRS indicators:

TABLE I
WITHIN-CLASS SIMILARITY OF OPTIMIZED TRAINING FEATURES FOR EACH MEASUREMENT MODE AND BIMANUAL CYCLICAL TASK

Subject		S1	S2	S3	S4	S5	S6	S7	S8	S9	S10	Mean	SD
EEG	In	0.589	0.496	0.643	0.441	0.833	0.439	0.393	0.272	0.424	0.478	0.500	0.155
		0.669	0.624	0.732	0.676	0.893	0.619	0.630	0.559	0.584	0.602	0.659	0.096
	90°	0.651	0.531	0.585	0.456	0.791	0.498	0.555	0.389	0.386	0.435	0.528	0.126
		0.701	0.659	0.699	0.660	0.844	0.671	0.727	0.567	0.571	0.589	0.669	0.083
	Anti	0.517	0.497	0.597	0.491	0.796	0.442	0.443	0.289	0.441	0.421	0.493	0.132
		0.636	0.650	0.705	0.653	0.852	0.627	0.655	0.564	0.585	0.580	0.651	0.082
fNIRS	In	0.056	-0.034	0.152	0.171	0.650	0.360	0.482	0.576	0.506	0.268	0.319	0.232
		0.513	0.732	0.570	0.510	0.836	0.694	0.596	0.522	0.650	0.808	0.643	0.121
	90°	0.281	0.408	0.372	0.194	0.304	0.268	0.386	0.256	0.502	0.507	0.348	0.105
		0.471	0.836	0.773	0.488	0.656	0.854	0.671	0.711	0.700	0.651	0.681	0.128
	Anti	0.337	0.351	0.470	0.416	0.676	0.398	0.450	0.531	0.650	0.625	0.490	0.124
		0.503	0.902	0.819	0.393	0.797	0.728	0.593	0.755	0.694	0.847	0.703	0.161

Table rows with white and gray background represent similarity calculated by the average and TRCA method, respectively.

TABLE II
DISCRIMINATION DEGREE OF TEST INDICATORS FOR EACH MEASUREMENT MODE AND BIMANUAL CYCLICAL TASK

Subject		S1	S2	S3	S4	S5	S6	S7	S8	S9	S10	Mean	SD
EEG	In	1.018	1.035	0.894	1.262	0.477	1.118	1.349	1.054	1.073	0.925	1.021	0.236
		1.821	1.539	2.257	1.710	2.744	1.493	1.884	0.981	1.159	1.225	1.681	0.532
	90°	1.020	1.009	0.861	1.243	0.489	1.146	1.304	1.081	1.060	0.933	1.015	0.228
		1.817	1.568	2.053	1.785	2.795	1.624	2.026	1.005	1.155	1.188	1.702	0.529
	Anti	1.103	1.017	0.850	1.260	0.506	1.076	1.320	1.057	1.038	0.911	1.014	0.227
		1.669	1.553	2.200	1.700	2.700	1.475	1.807	0.987	1.135	1.134	1.636	0.521
fNIRS	In	2.159	2.201	1.854	1.931	1.355	1.996	1.810	1.939	1.966	2.092	1.930	0.238
		2.222	3.418	2.434	2.147	1.931	1.576	1.796	2.360	2.363	1.481	2.172	0.550
	90°	2.120	1.978	1.908	1.938	1.687	1.938	1.895	2.180	1.880	1.969	1.949	0.134
		2.867	2.436	2.756	1.954	2.703	1.650	1.878	3.047	3.173	2.021	2.449	0.538
	Anti	2.084	1.955	1.838	2.017	1.372	1.958	1.765	1.996	1.861	1.984	1.883	0.203
		2.537	3.134	3.689	2.210	1.812	1.415	2.075	2.825	2.781	1.456	2.393	0.737

Table rows with white and gray background represent discrimination degree calculated by the average and TRCA method, respectively.

$F_{(2,29)} = 0.231$, $p = 0.795$). The obtained results demonstrated that the proposed indicators could reliably distinguish neural activities induced by different bimanual cyclical tasks, and the classification accuracy can be improved by combining EEG-fNIRS bimodal indicators.

IV. DISCUSSION

Real-time neurofeedback is crucial for constructing closed-loop bimanual rehabilitation systems. Reliable and timely characterization of neural activities can help refine bimanual training protocols for better rehabilitation outcomes. The main challenges in characterizing neural activation are the low SNR and high trial-to-trial variability of neural signals. The current study proposed a unified signal processing framework to characterize bimanual training-induced neural activities from single-trial EEG-fNIRS measurements. The effectiveness and robustness of our framework were verified in the following four aspects: 1) the differences between averaged EEG-fNIRS responses, 2) the within-class similarity of optimized features, 3) the discrimination degree of EEG-fNIRS bimodal indicators, and 4) the classification accuracy of bimanual cyclical tasks. These results are discussed in greater detail below.

According to Tettamanti *et al.*'s study [56], asymmetric bimanual movements require higher force output than symmetric bimanual movements. The differences are also reflected in upper-limb muscle activation and metabolic costs [57]. In this study, in-phase, 90° out-of-phase, and anti-phase bimanual cyclical tasks were employed, corresponding to symmetric, semi-asymmetric, and asymmetric bimanual movements, respectively. Participants were asked to perform these tasks with the custom-made bimanual rehabilitation robot in active-resisted mode. The EEG-fNIRS bimodal system was used to measure the brain oscillation and cerebral blood flow during robot-assisted bimanual training. The current study incorporated state-of-the-art denoising methods to reduce the interference of bimanual movement-induced motion and muscle artifacts. As illustrated in Fig. 6, significant changes in neural activation revealed by declines of μ band power and increases in HbO can be observed during bimanual cyclical tasks. In addition, the averaged neural responses of the anti-phase task were more prominent than that of in-phase and 90° out-of-phase. The distinguishable neural responses proved

the efficacy of our framework in signal denoising and feature extraction.

In this study, we used the TRCA method to extract bimanual task-related components from EEG-fNIRS bimodal features so that the neural responses can be analyzed at the single-trial level. As shown in Figs. 7. a & c, the similarity of within-class bimodal features was enhanced by TRCA, resulting in more reliable features and activation patterns. The improvement of within-class similarity can be observed for all bimanual cyclical tasks and measurement modes (see Table I). The optimized features were mapped into low-dimensional indicators to characterize bimanual movement-induced neural activities. Compared with high-dimensional features, low-dimensional indicators are more robust and easier to combine with other modal indicators (e.g., speed, acceleration, and muscle synergy) to form multimodal feedback. The high discrimination degree (see Table II) and classification accuracy (see Fig. 9) demonstrated that the low-dimensional could reliably characterize bimanual training-induced neural activities at the single-trial level. In addition, the SVM classification results revealed that fusion EEG and fNIRS bimodal indicators could achieve the highest accuracy (90.1%), which is in agreement with previous EEG-fNIRS bimodal studies [21], [23]–[25].

The overall results demonstrated that the proposed method could reliably characterize bimanual cyclical tasks at the single-trial level. Moreover, EEG-fNIRS bimodal measurements can provide more accuracy and robust neurofeedback. Several limitations need to be noted in this study. First is the limited number of human participants with unbalanced gender. Future study will consider recruiting a larger sample size of hemiparetic stroke patients. Second, the proposed method needs to be integrated into closed-loop rehabilitation systems and validated online.

V. Conclusion

This work proposed a unified signal processing framework to characterize bimanual cyclical tasks-induced neural activation from single-trail measurements. The extracted EEG and fNIRS features have been proved to characterize neural activation during robot-assisted bimanual training. Furthermore, the calculated indicators have good discrimination ability, and fusion of EEG and fNIRS indicators can improve bimanual cyclical task classification accuracy. In summary, these results confirmed that our method could characterize bimanual training-induced neural activation changes at the single-trail level and help construct robot-assisted bimanual rehabilitation systems with neurofeedback.

References

[1] Y. Vandermeeren *et al.*, "Bimanual motor skill learning and robotic assistance for chronic hemiparetic stroke: A randomized controlled trial," *Neural Regener. Res.*, vol. 16, no. 8, p. 1566, 2021.

[2] V. D. Tran, P. Dario, and S. Mazzoleni, "Kinematic measures for upper limb robot-assisted therapy following stroke and correlations with clinical outcome measures: A review," *Med. Eng. Phys.*, vol. 53, pp. 13–31, Mar. 2018.

[3] J. Wu, H. Cheng, J. Zhang, Z. Bai, and S. Cai, "The modulatory effects of bilateral arm training (BAT) on the brain in stroke patients: A systematic review," *Neurol. Sci.*, vol. 42, pp. 501–511, Nov. 2020.

[4] C. Duret, A.-G. Grosmaire, and H. I. Krebs, "Robot-assisted therapy in upper extremity hemiparesis: Overview of an evidence-based approach," *Frontiers Neurol.*, vol. 10, p. 412, Dec. 2019.

[5] Q. Miao *et al.*, "Performance-based iterative learning control for task-oriented rehabilitation: A pilot study in robot-assisted bilateral training," *IEEE Trans. Cognit. Develop. Syst.*, early access, Apr. 9, 2021, doi: 10.1109/TCDS.2021.3072096.

[6] C. Xu, S. Li, K. Wang, Z. Hou, and N. Yu, "Quantitative assessment of paretic limb dexterity and interlimb coordination during bilateral arm rehabilitation training," in *Proc. Int. Conf. Rehabil. Robot. (ICORR)*, Jul. 2017, pp. 634–639.

[7] A. Darzi, M. Gorsic, and D. Novak, "Difficulty adaptation in a competitive arm rehabilitation game using real-time control of arm electromyogram and respiration," in *Proc. Int. Conf. Rehabil. Robot. (ICORR)*, Jul. 2017, pp. 857–862.

[8] S. K. Subramanian, J. Yamanaka, G. Chilingaryan, and M. F. Levin, "Validity of movement pattern kinematics as measures of arm motor impairment poststroke," *Stroke*, vol. 41, no. 10, pp. 2303–2308, Oct. 2010.

[9] C. Duret, O. Courtial, and A. G. Grosmaire, "Kinematic measures for upper limb motor assessment during robot-mediated training in patients with severe sub-acute stroke," *Restorative Neurol. Neurosci.*, vol. 34, no. 2, pp. 237–245, Mar. 2016.

[10] F. Grimm, G. Naros, and A. Gharabaghi, "Closed-loop task difficulty adaptation during virtual reality reach-to-grasp training assisted with an exoskeleton for stroke rehabilitation," *Frontiers Neurosci.*, vol. 10, p. 518, Nov. 2016.

[11] Y. Huang, W. P. Lai, Q. Qian, X. Hu, E. W. C. Tam, and Y. Zheng, "Translation of robot-assisted rehabilitation to clinical service: A comparison of the rehabilitation effectiveness of EMG-driven robot hand assisted upper limb training in practical clinical service and in clinical trial with laboratory configuration for chronic stroke," *Biomed. Eng. OnLine*, vol. 17, no. 1, pp. 1–17, Dec. 2018.

[12] Q. Qian, X. Hu, Q. Lai, S. C. Ng, Y. Zheng, and W. Poon, "Early stroke rehabilitation of the upper limb assisted with an electromyography-driven neuromuscular electrical stimulation-robotic arm," *Frontiers Neurol.*, vol. 8, p. 447, Sep. 2017.

[13] C. Calautti and J.-C. Baron, "Functional neuroimaging studies of motor recovery after stroke in adults: A review," *Stroke*, vol. 34, no. 6, pp. 1553–1566, Jun. 2003.

[14] P. Langhorne, J. Bernhardt, and G. Kwakkel, "Stroke rehabilitation," *Lancet*, vol. 377, no. 9778, pp. 1693–1702, May 2011.

[15] F. L. da Silva, "EEG and MEG: Relevance to neuroscience," *Neuron*, vol. 80, no. 5, pp. 1112–1128, 2013.

[16] X. Cui, S. Bray, D. M. Bryant, G. H. Glover, and A. L. Reiss, "A quantitative comparison of NIRS and fMRI across multiple cognitive tasks," *NeuroImage*, vol. 54, no. 4, pp. 2808–2821, Feb. 2011.

[17] M. Gandolfi *et al.*, "Quantification of upper limb motor recovery and EEG power changes after robot-assisted bilateral arm training in chronic stroke patients: A prospective pilot study," *Neural Plasticity*, vol. 2018, pp. 1–15, Mar. 2018.

[18] C. Li, Y. Inoue, T. Liu, and L. Sun, "Validation of bimanual-coordinated training supported by a new upper-limb rehabilitation robot: A near-infrared spectroscopy study," *Disab. Rehabil., Assistive Technol.*, vol. 8, no. 1, pp. 38–48, Jan. 2013.

[19] C. Li, J. Li, Y. Inoue, and T. Liu, "Verification of additional merits of a bimanual-coordinated rehabilitation robot using near-infrared spectroscopic technology," *Adv. Robot.*, vol. 28, no. 14, pp. 955–965, Jul. 2014.

[20] N. Richer, R. J. Downey, W. D. Hairston, D. P. Ferris, and A. D. Nordin, "Motion and muscle artifact removal validation using an electrical head phantom, robotic motion platform, and dual layer mobile EEG," *IEEE Trans. Neural Syst. Rehabil. Eng.*, vol. 28, no. 8, pp. 1825–1835, Aug. 2020.

[21] S. Ge *et al.*, "A brain-computer interface based on a few-channel EEG-fNIRS bimodal system," *IEEE Access*, vol. 5, pp. 208–218, 2017.

[22] R. A. Ramadan and A. V. Vasilakos, "Brain computer interface: Control signals review," *Neurocomputing*, vol. 223, pp. 26–44, Feb. 2017.

[23] Y.-C. Jiang, P. Wang, H. Liu, and S. Ge, "Decoding action observation using complex brain networks from simultaneously recorded EEG-fNIRS signals," in *Proc. 26th Int. Conf. Neural Inf. Process. (ICONIP)*, Sydney, NSW, Australia. Switzerland: Springer, 2019, pp. 559–569.

[24] M. Abtahi *et al.*, "Merging fNIRS-EEG brain monitoring and body motion capture to distinguish Parkinsons disease," *IEEE Trans. Neural Syst. Rehabil. Eng.*, vol. 28, no. 6, pp. 1246–1253, Jun. 2020.

[25] X. Yin *et al.*, "A hybrid BCI based on EEG and fNIRS signals improves the performance of decoding motor imagery of both force and speed of hand clenching," *J. Neural Eng.*, vol. 12, no. 3, Jun. 2015, Art. no. 036004.
[26] S. Ge *et al.*, "Neural activity and decoding of action observation using combined EEG and fNIRS measurement," *Frontiers Hum. Neurosci.*, vol. 13, p. 357, Oct. 2019.
[27] A. Berger, N. H. Pixa, F. Steinberg, and M. Doppelmayr, "Brain oscillatory and hemodynamic activity in a bimanual coordination task following transcranial alternating current stimulation (tACS): A combined EEG-fNIRS study," *Frontiers Behav. Neurosci.*, vol. 12, p. 67, Apr. 2018.
[28] J. Choe, B. A. Coffman, D. T. Bergstedt, M. D. Ziegler, and M. E. Phillips, "Transcranial direct current stimulation modulates neuronal activity and learning in pilot training," *Frontiers Hum. Neurosci.*, vol. 10, p. 34, Feb. 2016.
[29] B. Blankertz, S. Lemm, M. Treder, S. Haufe, and K.-R. Müller, "Single-trial analysis and classification of ERP components—A tutorial," *NeuroImage*, vol. 56, no. 2, pp. 814–825, May 2011.
[30] W. A. Truccolo, M. Ding, K. H. Knuth, R. Nakamura, and S. L. Bressler, "Trial-to-trial variability of cortical evoked responses: Implications for the analysis of functional connectivity," *Clin. Neurophysiol.*, vol. 113, no. 2, pp. 206–226, Feb. 2002.
[31] R. Coppola, R. Tabor, and M. S. Buchsbaum, "Signal to noise ratio and response variability measurements in single trial evoked potentials," *Electroencephalogr. Clin. Neurophysiol.*, vol. 44, no. 2, pp. 214–222, Feb. 1978.
[32] S. Ge *et al.*, "Sinusoidal signal assisted multivariate empirical mode decomposition for brain–computer interfaces," *IEEE J. Biomed. Health Informat.*, vol. 22, no. 5, pp. 1373–1384, Sep. 2018.
[33] U. Asgher, R. Ahmad, N. Naseer, Y. Ayaz, M. J. Khan, and M. K. Amjad, "Assessment and classification of mental workload in the prefrontal cortex (PFC) using fixed-value modified Beer-Lambert law," *IEEE Access*, vol. 7, pp. 143250–143262, 2019.
[34] H. Nazeer *et al.*, "Enhancing classification accuracy of fNIRS-BCI using features acquired from vector-based phase analysis," *J. Neural Eng.*, vol. 17, no. 5, Oct. 2020, Art. no. 056025.
[35] H. Takana, T. Katura, and H. Sato, "Task-related component analysis for functional neuroimaging and application to near-infrared spectroscopy data," *NeuroImage*, vol. 64, pp. 308–327, Jan. 2013.
[36] Q. Miao, Y. Peng, L. Liu, A. McDaid, and M. Zhang, "Subject-specific compliance control of an upper-limb bilateral robotic system," *Robot. Auto. Syst.*, vol. 126, Apr. 2020, Art. no. 103478.
[37] C. Sun *et al.*, "Bilateral asymmetry of hand force production in dynamic physically-coupled tasks," *IEEE J. Biomed. Health Informat.*, early access, Sep. 14, 2021, doi: 10.1109/JBHI.2021.3112201.
[38] M. Kleiner, D. Brainard, and D. Pelli, "What's new in psychtoolbox-3?" *Perception*, vol. 36, pp. 1–16, Jan. 2007.
[39] T. D. Lee, S. P. Swinnen, and S. Verschueren, "Relative phase alterations during bimanual skill acquisition," *J. Motor Behav.*, vol. 27, no. 3, pp. 263–274, Sep. 1995.
[40] F. Debaere, N. Wenderoth, S. Sunaert, P. Van Hecke, and S. P. Swinnen, "Cerebellar and premotor function in bimanual coordination: Parametric neural responses to spatiotemporal complexity and cycling frequency," *NeuroImage*, vol. 21, no. 4, pp. 1416–1427, Apr. 2004.
[41] L. Koessler *et al.*, "Automated cortical projection of EEG sensors: Anatomical correlation via the international 10–10 system," *NeuroImage*, vol. 46, no. 1, pp. 64–72, May 2009.
[42] N. Richer, R. J. Downey, A. D. Nordin, W. D. Hairston, and D. P. Ferris, "Adding neck muscle activity to a head phantom device to validate mobile EEG muscle and motion artifact removal," in *Proc. 9th Int. IEEE/EMBS Conf. Neural Eng. (NER)*, Mar. 2019, pp. 275–278.
[43] G. A. Z. Morais, J. B. Balardin, and J. R. Sato, "fNIRS Optodes' location decider (fOLD): A toolbox for probe arrangement guided by brain regions-of-interest," *Sci. Rep.*, vol. 8, no. 1, pp. 1–11, Dec. 2018.
[44] A. Gramfort *et al.*, "MEG and EEG data analysis with MNE-Python," *Frontiers Neurosci.*, vol. 7, p. 267, Dec. 2013.
[45] C. A. E. Kothe and T.-P. Jung, "Artifact removal techniques with signal reconstruction," U.S. Patent 14/895 440, Apr. 28, 2016.
[46] A. Hyvärinen, "Fast and robust fixed-point algorithms for independent component analysis," *IEEE Trans. Neural Netw.*, vol. 10, no. 3, pp. 626–634, May 1999.
[47] L. Pollonini, C. Olds, H. Abaya, H. Bortfeld, M. S. Beauchamp, and J. S. Oghalai, "Auditory cortex activation to natural speech and simulated cochlear implant speech measured with functional near-infrared spectroscopy," *Hearing Res.*, vol. 309, pp. 84–93, Mar. 2014.
[48] L. Kocsis, P. Herman, and A. Eke, "The modified Beer–Lambert law revisited," *Phys. Med. Biol.*, vol. 51, no. 5, pp. N91–N98, Mar. 2006.
[49] F. A. Fishburn, R. S. Ludlum, C. J. Vaidya, and A. V. Medvedev, "Temporal derivative distribution repair (TDDR): A motion correction method for fNIRS," *NeuroImage*, vol. 184, pp. 171–179, Jan. 2019.
[50] G. Pfurtscheller, C. Brunner, A. Schlögl, and F. H. Lopes da Silva, "Mu rhythm (de) synchronization and EEG single-trial classification of different motor imagery tasks," *NeuroImage*, vol. 31, no. 1, pp. 153–159, May 2006.
[51] S. Makeig, "Auditory event-related dynamics of the EEG spectrum and effects of exposure to tones," *Electroencephalogr. Clin. Neurophysiol.*, vol. 86, no. 4, pp. 283–293, Apr. 1993.
[52] A. de Cheveigné and D. Arzounian, "Robust detrending, rereferencing, outlier detection, and inpainting for multichannel data," *NeuroImage*, vol. 172, pp. 903–912, May 2018.
[53] H. Tanaka, T. Katura, and H. Sato, "Task-related oxygenation and cerebral blood volume changes estimated from NIRS signals in motor and cognitive tasks," *NeuroImage*, vol. 94, pp. 107–119, Jul. 2014.
[54] M. Nakanishi, Y. Wang, X. Chen, Y. Wang, X. Gao, and T.-P. Jung, "Enhancing detection of SSVEPs for a high-speed brain speller using task-related component analysis," *IEEE Trans. Biomed. Eng.*, vol. 65, no. 1, pp. 104–112, Jan. 2018.
[55] F. Duan, H. Jia, Z. Sun, K. Zhang, Y. Dai, and Y. Zhang, "Decoding premovement patterns with task-related component analysis," *Cognit. Comput.*, vol. 13, no. 5, pp. 1389–1405, Sep. 2021.
[56] A. Tettamanti, M. Giordano, and R. Gatti, "Effects of coupled upper limbs movements on postural stabilisation," *J. Electromyogr. Kinesiol.*, vol. 23, no. 5, pp. 1222–1228, Oct. 2013.
[57] A. D. Nordin, W. D. Hairston, and D. P. Ferris, "Faster gait speeds reduce alpha and beta EEG spectral power from human sensorimotor cortex," *IEEE Trans. Biomed. Eng.*, vol. 67, no. 3, pp. 842–853, Mar. 2020.